Convective Gusts Nowcasting Based on Radar Reflectivity and a Deep Learning Algorithm

Haixia Xiao[1], Yaqiang Wang[2,*], Yu Zheng[1,*], Yuanyuan Zheng[1], Xiaoran Zhuang[1,3], Hongyan Wang[2], and Mei Gao[2]

[1]Key Laboratory of Transportation Meteorology of China Meteorological Administration, Nanjing Joint Institute for Atmospheric Sciences, Nanjing 210041, China
[2]Chinese Academy of Meteorological Sciences, Beijing 100081, China
[3]Jiangsu Meteorological Observatory, Nanjing 210041, China
[*]These authors contributed equally to this work.

Correspondence: Yangqiang Wang (yqwang@cma.gov.cn), Yu Zheng (zhengyu@cma.gov.cn)

Abstract.

Convective wind gusts (CGs) are usually related to thunderstorms, and they may cause great structural damage and serious hazards, such as train derailment, service interruption, and building collapse. Due to the small-scale and nonstationary nature of CGs, reliable CGs nowcasting with high spatial and temporal resolutions has remained unattainable. In this study, a novel nowcasting model based on deep learning - namely, CGsNet - is developed for 0-2 h of quantitative CGs nowcasting, first achieving minute-kilometer-level forecasts. CGsNet is a physics-constrained model established by training on large corpora of average surface wind speed (ASWS) and radar observations, it can produce realistic and spatiotemporally consistent ASWS predictions in CGs events. By combining the gust factor (1.77, the ratio of the observed peak wind gust speed (PWGS) to the ASWS) with the ASWS predictions, the PWGS forecasts are estimated with a spatial resolution of $0.01° \times 0.01°$ and a 6-minute temporal resolution. CGsNet is shown to be effective, and it has an essential advantage in learning the spatiotemporal features of CGs. In addition, quantitative evaluation experiments indicate that CGsNet exhibits higher generalization performance for CGs than the traditional nowcasting method based on numerical weather prediction models. CGs nowcasting technology can be applied to provide real-time quantitative CGs forecasts and alerts the damaging wind events in meteorological services.

1 Introduction

Convective wind gusts (CGs) are nontronadic, straight-line winds (Mohr et al., 2017; Yu and Zheng, 2020). They predominantly occur in Eastern China in the warm summer months (Yang et al., 2017), and they are usually associated with thunderstorm clouds, in particular squall lines and supercells, which generate conditions conducive to the appearance of whirlwinds and squalls (Kolendowicz et al., 2016). Severe convective gusts are caused either by mesoscale cold pools associated with horizontal pressure gradients large enough to produce high wind speeds in the absence of strong downdrafts or by local-scale downbursts that create strong divergent horizontal winds near the ground (Wakimoto, 2001). These severe convective gusts may cause

Geoscientific
Model Development
Discussions

considerable damage to communication, transport, buildings and other structures, and even the health and life of humans in many parts of the world (Mohr et al., 2017; Wang et al., 2020).

CGs as defined by the China Meteorological Administration (CMA) are usually recognized as a PWGS $\geq$ 17.2 m/s caused by severe atmospheric convection (Yu and Zheng, 2020). Compared with large-scale wind storms, many observations show

25 that convectively induced storm events can reach higher wind speeds (Mohr et al., 2017). For example, the CGs observed in 1983 during a microburst in the United States had a peak gust of 67 m/s (Fujita, 1990), for which wind speeds are comparable to those of an F3 tornado based on damage assessments. Thus, forecasting the occurrence of CGs in advance is valuable for reducing the risk and threat of damaging wind events.

Currently, accurate CGs nowcasting is still a challenging issue in operational meteorology despite its severe impact (Ray,

30 2015; Stensrud et al., 2009). This is primarily for several reasons. One is the small-scale and nonstationary nature of CGs. Due to the rapid evolution of fine-scale convective systems and their complicated interactions with environmental features, it is difficult for mesoscale numerical models or statistical models to capture and forecast CGs. In addition, the sparsity of wind observations is a factor that hinders the development and verification of gust nowcasting models. The most frequently cited record-breaking wind speeds are usually associated with wind gust values. This refers to a maximum momentary (2-3 sec.)

35 wind speed that exceeds the 2-minute mean wind speed by at least 5 m/s (WMO, 2010). At present, wind gusts between full hours of observation have been recorded in Eastern China, which makes it possible to determine the actual maximum wind gusts/peak wind gusts (PWGS) for each hour. Obviously, these existing meteorological observation networks cannot record fine-scale CGs accurately (Kahl et al., 2021; Mohr et al., 2017), and a significant portion of the highest wind gusts may be missing.

40 Many previous studies have mainly focused on potential severe convective weather (SCW) forecasting (McNulty, 1995; Doswell et al., 1996) or the possibility of classified SCW forecasting (Zhou et al., 2019; Lagerquist et al., 2017), while quantitative CGs nowcasting has rarely been reported. Currently, some studies focus on wind gust forecasting by using physically based methods, empirical results and tuning, statistical analysis or machine learning methods (Kahl, 2020; Kahl et al., 2021; Lei et al., 2009; Sheridan, 2018; Nerini et al., 2014; Chaudhuri and Middey, 2011). Although some progress has been made in

45 these studies, their performance on wind gust nowcasting (0-2 h) is poor (Wang et al., 2016), especially in terms of spatial and temporal resolution. For example, the wind forecasted by Integrated Nowcasting through Comprehensive Analysis (INCA) (Haiden et al., 2011) or the newly developed meteorologically stratified gust factor (MSGF) model (Kahl et al., 2021) has a 1-hour temporal resolution, which is not sufficient for describing the evolution of wind gusts. Most importantly, few gust forecasting models have been evaluated for effectiveness in CGs nowcasting.

50 Recent advances in deep learning (Yang et al., 2017), especially recurrent neural networks (RNNs) and convolutional neural networks (CNNs), have provided some useful insights into the meteorological field (Duan et al., 2021; Sadeghi et al., 2020). Many approaches based on RNNs and CNNs have been applied successfully to short-term weather forecasting due to their ability to capture temporal and spatial variations in image features, e.g., short-term drought (Danandeh Mehr et al., 2022) and quantitative precipitation forecasts (Shi et al., 2015). An evaluation of the applications indicates that the deep learning solutions

55 can model complex nonlinear systems and better extract advanced features.

Geoscientific
Model Development
Discussions

Complex physical processes and dynamic characteristics are often involved in convective systems at small spatial and temporal scales (Doswell, 2001). It is critical to fully extract convective characteristics automatically to improve the forecast accuracy, and deep learning provides a practical tool for this purpose. In particular, Zhou et al. (2019) developed a forecasting solution for SCW using a CNN, producing objective-possibility forecasting products. Their results showed that deep learning

60   methods achieve better performance than traditional forecasting methods. Thus, as it is a similar problem, deep learning may have considerable application potential in CGs nowcasting, and it is promising to test CGs forecasting using deep learning methods, which has rarely been documented before.

The objective of this study is to achieve quantitative nowcasting of CGs speed in eastern China using the deep learning method, in principle down to the minute-level timescale. Doppler weather radar is an important device for observing and

65   forecasting CGs because of abundant weather information in radar reflectivity (e.g., bow echo and hook echo) (Holleman, 2001; Yuan et al., 2018; Yu and Zheng, 2020). Thus, in this study, we aim to forecast quantitative CGs based on observed wind and radar data, which has rarely been considered in previous studies. We also compare the nowcasting performance of the deep learning method with that of the INCA approach. Notably, we concentrate on the nowcasting and evaluation of the average surface wind speed (ASWS) and PWGS, which are both key factors that reflect the strength and influence of CGs. We believe

70   this work will have significant application potential in small-scale hazard assessment and alerting of threats to the economy and human activities.

2   Data

The study area is in Eastern China (Figure 1), including Jiangsu Province and its adjacent area. The latitudinal and longitudinal ranges of the study area are 30.4°N–35.2°N and 116.33°E–121.93°E, respectively. Considering that CGs associated with

75   thunderstorms occur predominantly in the warm season in eastern China (Yang et al., 2017), April to September of each year was selected as the period of the experiments in this study.

2.1   Wind data

For the ground-truth reference, the ASWS data comprise in situ observations with a 5-minute time interval, which is the 2-minute average of the 3-second wind measured using automatic weather stations (AWSs) (Figure 1b) at a height of 10 meters

80   above the ground. Note that there are few wind observation data on the seacoast. To match the spatiotemporal resolution of the observed radar reflectivity mosaics (RMOSs), the ASWS data were first interpolated to 6 minutes using linear interpolation. Inverse distance-weighted (IDW) interpolation has the advantages of being fast to calculate and easy to understand, and it is suitable for eastern China, where the automatic stations are dense and evenly distributed. Then, the IDW interpolation method was employed to regrid the ASWS data to a spatial resolution of $0.01° \times 0.01°$ by using the four nearest stations within 15 km

85   with a power of 2. In this study, the interpolated wind data are assumed to be close to the true observed wind field.

ASWS data from 2016 to 2022 were considered. To further select ASWS data associated with CGs, the samples were selected using two principles: 1) more than 2% of stations recorded ASWS > 10.8 m/s; and 2) the precipitation at more than 5% of the stations within an hour was greater than 0.1 mm.

In addition, observed peak wind gust speed (PWGS) from 2021 to 2022 was used in this study for subsequent gust factor calculation and model evaluation; it is the maximum 3-second average gust recorded over 1 hour by the AWS.

2.2 Radar reflectivity

Weather radar provides a highly detailed representation of the spatial structure and temporal evolution of thunderstorms over a large area (Knupp, 1987). Weather radar data may also indicate the time and location of the CGs that occurred (Holleman, 2001). Thus, the constant-altitude radar RMOSs at 3 km are used as auxiliary data along with observed wind data to forecast the speed of CGs. The RMOS data is from 10 weather radar stations in eastern China (Figure 1a). The type of radar sensor is the CINRAD/SA Doppler weather radar (Sheng et al., 2006). The RMOS is determined by projecting the base reflectivity factor onto equal longitude and latitude coordinates. The time interval of the RMOS data is 6 minutes, the spatial resolution is 0.01°, and the grid data are arranged from west to east and north to south.
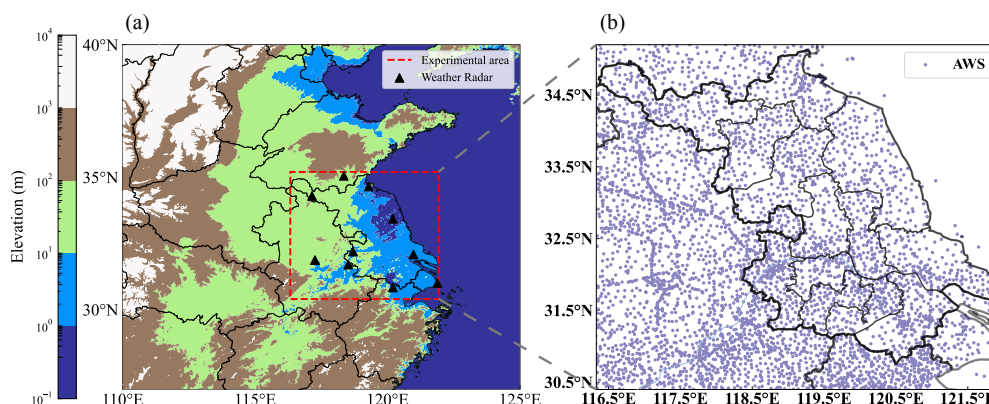

Figure 1. The selected study area: the red dotted line in (a) represents Eastern China (30.4°N–35.2°N, 116.33°E–121.93°E); the black triangles in (a) represent the locations of the weather radar; and the purple dots in (b) are the locations of the AWSs that currently measure ASWS and PWGS.

2.3 Workflow

The workflow of this study is illustrated in Figure 2. First, the RMOS data were preprocessed, and the ASWS data were interpolated and regridded as mentioned above. Second, the spatial-temporal resolutions of the RMOS and ASWS samples were matched, and the time of the RMOS samples was determined by the selected ASWS samples. Third, the dataset was divided into three parts (training, validation and testing datasets) according to the observation time. Fourth, the ASWS data

4

were clipped to between 0 and 35 m/s and subsequently normalized to the range [0.0, 1.0] through min-max normalization.

105 Similarly, the RMOS values were clipped to between 0 and 70 dBZ and subsequently normalized to between 0 and 1. Fifth, the ASWS and RMOS data in the past 60 minutes were used as input data to train and validate the deep learning nowcasting model, and the outputs were the forecasted ASWS and RMOS with lead times of 6-120 minutes ahead, with a spatial resolution of $0.01° \times 0.01°$ and a 6-minute temporal resolution. Sixth, the performance of the deep learning model in forecasting ASWS was evaluated by different statistical variables. Seventh, the mean gust factor (GF) was determined by comparing the observed

110 PWGS and ASWS. Subsequently, the PWGS forecasts were estimated by multiplying the GF by the forecasted ASWS. Finally, the PWGS forecasts were compared with INCA results, and two cases were also showed to demonstrate the accuracy of PWGS forecasts.
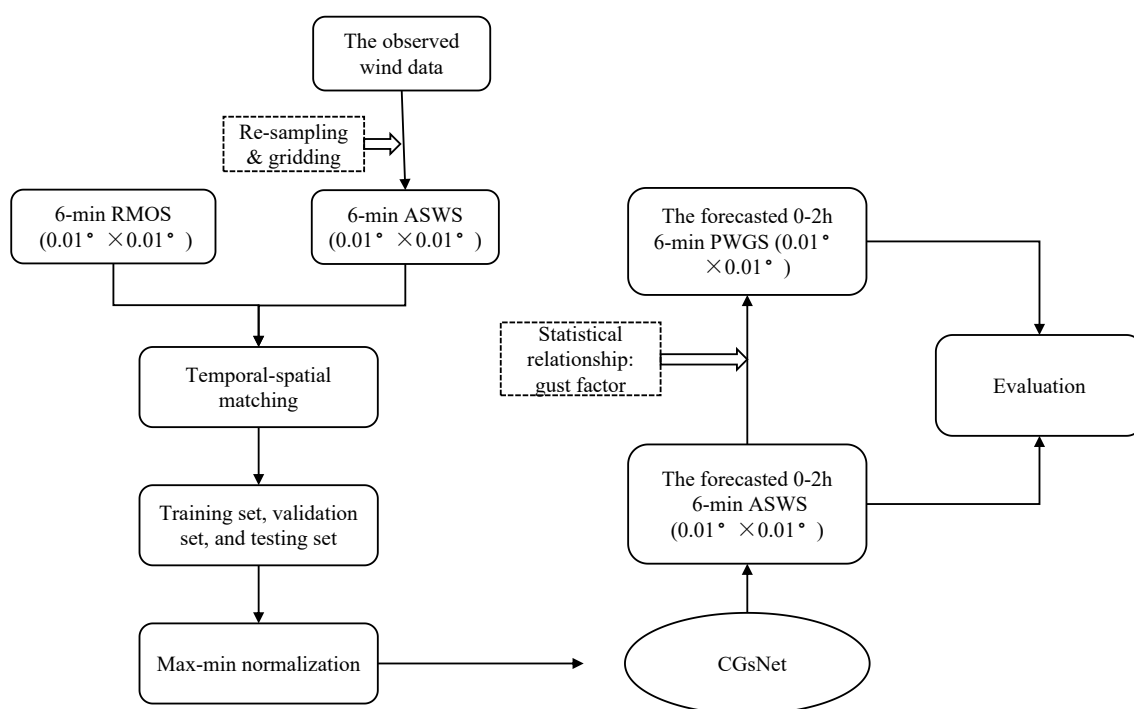
Figure 2. Workflow of deep learning model-based CGs nowcasting.

3 Model and settings

3.1 Model architecture

115 We started by adapting the network structure proposed by Guen and Thome (2020b), namely, PhyDNet, which is a sequence-to-sequence network. Unlike traditional networks, it has a two-branch deep architecture, i.e., the newly proposed recurrent physical cell (PhyCell) and ConvLSTM. Specifically, PhyCell is inspired by data assimilation techniques for performing partial differential equation (PDE)-constrained prediction in latent space. It explicitly disentangles PDE dynamics from unknown complementary information and allows for a generic class of linear PDEs through varying differential orders, e.g., wave equa-

120 tions. In PhyDNet, the physical knowledge is represented by PDEs, which can enforce physical constraints for future image prediction well. PhyDNet has been successfully employed in many fields, e.g., solar irradiance forecasting using fisheye images (Guen and Thome, 2020a) and nitrogen prediction (Jahanbakht et al., 2022).

The attention mechanism can focus on the important information among a large amount of input information and ignore most of the unimportant information (Niu et al., 2021). Thus, an attention mechanism is applied to improve the performance

125 of PhyDNet for nowcasting CGs in this study. Here, the PhyDNet with an attention mechanism for CGs nowcasting is called CGsNet, and its architecture is illustrated in Figure 3. An input sequence $\{x_{t-K}^{a,r}, \ldots, x_t^{a,r}\} \in \mathbb{R}^{K \times n \times m \times c}$ including ASWS (a) and RMOS (r) with spatial size $n \times m$ and c channels is projected into $\{h_{t-K}^E, \ldots, h_t^E\}$ by the convolutional units and processed by the recurrent block unfolded in time. This forms a sequence-to-sequence architecture suited for multistep prediction, outputting T future CGs predictions $\{\hat{x}_{t+1}^{a,r}, \ldots, \hat{x}_{t+T}^{a,r}\}$. For time t, we learn a weight vector $\langle \alpha_{t1}, ..., \alpha_{tk} \rangle$ for K hidden

130 states $\{h_{t-K}^m, \ldots, h_{t-1}^m\}$, where the weight α_{tk} can be interpreted as the relative importance of the k-th h^m. Each weight α_{tk} is computed by taking h_t^E as input, followed by a softmax operation. Then, we perform summation over the weighted hidden states to obtain an attention representation A_t, which will be incorporated into the decoder for prediction. The key equations for generating the attention representation A_t for the $t+1$-th output prediction are summarized as follows.

$$s_{tk} = W * h_t^E + b, \quad \forall k \in [1, K] \tag{1}$$

135
$$\alpha_{tk} = \frac{\exp(s_{tk})}{\sum_{k=1}^{K} \exp(s_{tk})}, \quad \forall k \in [1, K] \tag{2}$$

$$A_t = \sum_{k=1}^{K} \alpha_{tk} h_k^m \tag{3}$$

$$h_{t+1}^D = PhyCell([h_t^E, A_t]) + ConvLSTM([h_t^E, A_t]) \tag{4}$$

where '$*$' denotes the convolution operator and the kernel matrices W and biases b are parameters to be learned. The high-level representation h_{t+1}^D is then fed into the deconvolutional units, and $\hat{x}_{t+1}^{a,r}$ is calculated. Similarly, by inputting $\hat{x}_{t+1}^{a,r}$ into

140 the decoder, combined with the attention mechanism, the forecasted $\hat{x}_{t+2}^{a,r}$ can be calculated. In this cycle, we can obtain the ASWS and RMOS forecasts in the future, i.e., $\{\hat{x}_{t+1}^{a,r}, \ldots, \hat{x}_{t+n}^{a,r}\}$. This attention mechanism operation can better model both short-term and long-term dependencies.
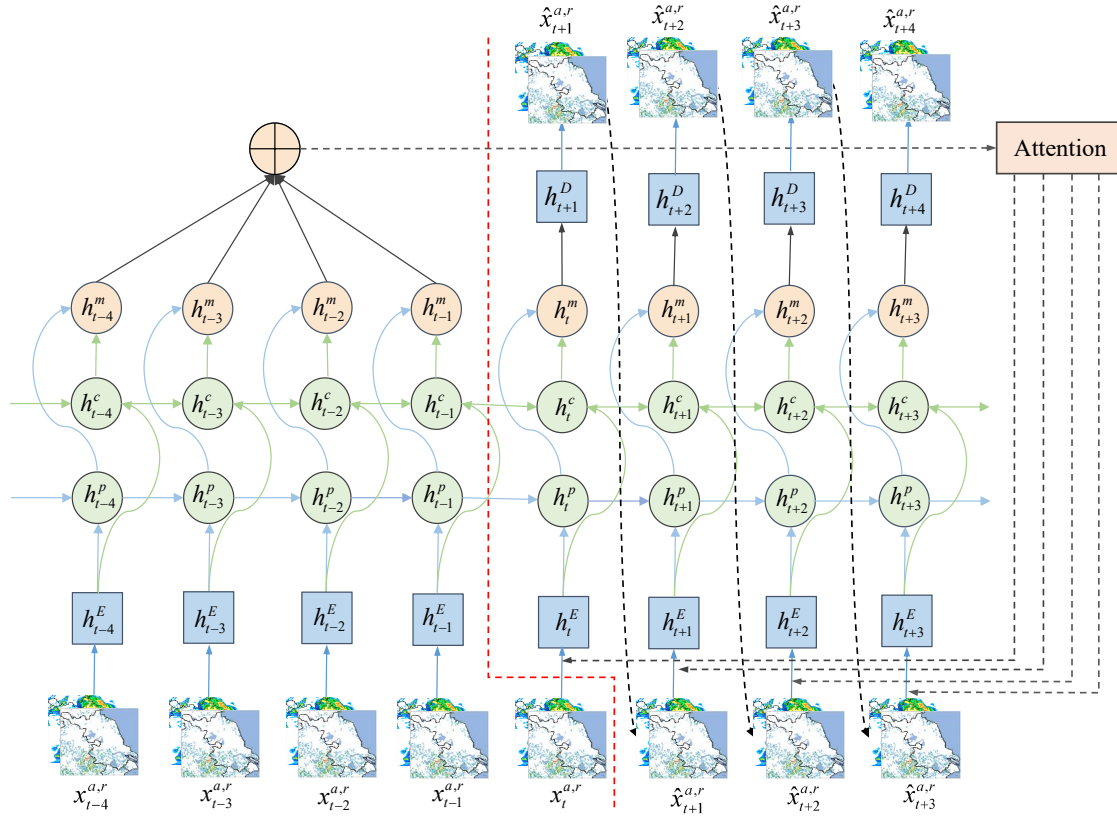
Figure 3. Illustration of CGsNet. The encoder is to the left of the dotted red line, and the decoder is to the right. $x_i^{a,r}$ and $\hat{x}_i^{a,r}$ are the observed and forecasted ASWS/RMOS fields, respectively. h_i^E and h_i^D indicate the input and output tensors calculated by the convolution and deconvolution units, respectively. h_i^c and h_i^p indicate the hidden states of ConvLSTM and PhyCell, respectively. h_i^m represents the hidden state that combines the values from h_i^c and h_i^p.

3.2 Experimental settings

Here, we aim to forecast 0-2 hour CGs; thus, 10 historical ASWS and RMOS grid fields $\{x_1^{a,r},\ldots,x_{10}^{a,r}\} \in \mathbb{R}^{10 \times 480 \times 560 \times 2}$

145 were taken as the inputs, and the subsequent 20 ASWS and RMOS grid fields $\{x_{11}^{a,r},\ldots,x_{30}^{a,r}\} \in \mathbb{R}^{20 \times 480 \times 560 \times 2}$ were the ground-truth outputs. The ASWS and RMOS grid fields from 2016 to 2020 were used for model's training and validation, and the fields in 2021 and 2022 were employed for ASWS testing and PWGS testing, respectively. Correspondingly, we obtained 15,629 CGs samples, including a training set of 13,155 samples, a validation set of 1,236 samples, and the testing sets of 1,184 and 54 samples for ASWS and PWGS.

150 Regarding the training settings, Adam (Kingma and Ba, 2014) was used as the optimizer, and the batch size was set as 2. The learning rate was initially set to 0.001 and then multiplied by 0.3 if the loss did not decrease when the model was trained for 2 epochs. The model was trained for a total of 50 epochs, and the model weight with the minimum loss on the validation

set was saved. The comparison and evaluation experiments were implemented on the testing set. All experiments in this study were conducted using Python and PyTorch and executed on 4 NVIDIA GeForce RTX 3090 GPUs with the CUDA-11.1 library.

155 ## 3.3 Loss function

The loss function is used to adjust the weights of the deep learning model, and it is an instructive function that guides how to improve the weight coefficients. Most previous studies used the mean absolute error (MAE) loss or mean squared error (MSE) loss as the default to train their models (Tran and Song, 2019; Veillette et al., 2020; Franch et al., 2020). However, these losses will result in smoothing effects in the predicted fields, since they may make a good assumption about the global similarity of

160 the two fields, meaning that the field's details may be lost (Tran and Song, 2019; Franch et al., 2020). Notably, with increasing forecast time, the problem of underestimating high values becomes more obvious, such as underestimating heavy rain or radar reflectivity. To address these problems and make the predictions sharper and more realistic, the weighted MAE loss (Shi et al., 2017) was adopted in this study. The weight for the MAE loss function is shown in Table 1, and it is set according to the six ASWS and RMOS value ranges. The weighted MAE loss is equivalent to data augmentation, as it gives a large weight to strong

165 gusts and a small weight to weak gusts. Thus, this setting has a better effect on forecasting CGs than loss without weights. The weighted loss function can be calculated as follows.

$$loss = \frac{1}{N} \sum_{n=1}^{N} \sum_{i=1}^{480} \sum_{j=1}^{560} w_{n,i,j} \left| y_{n,i,j}^a - \hat{y}_{n,i,j}^a \right| + \frac{1}{N} \sum_{n=1}^{N} \sum_{i=1}^{480} \sum_{j=1}^{560} w_{n,i,j} \left| y_{n,i,j}^r - \hat{y}_{n,i,j}^r \right| \tag{5}$$

where N is the number of samples, and i and j are the width and length of the ASWS/RMOS, respectively. Moreover, $y_{n,i,j}^a$, $y_{n,i,j}^r$, $\hat{y}_{n,i,j}^a$, and $\hat{y}_{n,i,j}^r$ are the observed ASWS, observed RMOS, forecasted ASWS and forecasted RMOS values, respectively.

170 $w_{n,i,j}^a$ and $w_{n,i,j}^r$ denote the weights of the ASWS and RMOS values, respectively.

Table 1. The weights of the ASWS and RMOS in the MAE loss.

Wind (m/s)	Weights	RMOS (dBZ)	Weights
y ≤ 5.5	0.5	y ≤ 15	0.5
5.5 ≤ y ≤ 8.0	1	15 ≤ y ≤ 25	1
8.0 ≤ y ≤ 13.9	2	25 ≤ y ≤ 35	2.5
13.9 ≤ y ≤ 17.2	10	35 ≤ y ≤ 45	5
17.2 ≤ y ≤ 20.8	20	45 ≤ y ≤ 50	10
y ≥ 20.8	30	y ≥ 50	15

3.4 Model evaluation

To quantify the capabilities of CGsNet, the critical success index (CSI), probability of detection (POD), false alarm rate (FAR), bias score, and Heidke skill score (HSS) were implemented for evaluating the CGsNet forecasts. The following equations

Geoscientific
Model Development
Discussions

describe these indices.

$$CSI = \frac{TP}{TP + FP + FN} \tag{6}$$

$$POD = \frac{TP}{TP + FN} \tag{7}$$

$$FAR = \frac{FP}{TP + FP} \tag{8}$$

$$BIAS = \frac{TP + FP}{TP + FN} \tag{9}$$

$$HSS = \frac{(TP \times TN - FN \times FP)}{(TP + FN) \times (FN + TN) + (TP + FP) \times (FP + TN)} \tag{10}$$

where TP, TN, FN, and FP are the numbers of true positives, true negatives, false negatives, and false positives, respectively. Moreover, the MAE and RMSE are also used for model evaluation, and are calculated as follows.

$$MAE = \frac{1}{Q} \sum_{i=1}^{Q} |y_i - \hat{y}_i| \tag{11}$$

$$RMSE = \sqrt{\frac{1}{Q} \sum_{i=1}^{Q} (y_i - \hat{y}_i)^2} \tag{12}$$

where Q is the number of predicted ASWS pixel values. y_i and $\hat{y}_i$ represent the observations and forecasts, respectively. Note that the value of BIAS is greater than 0, and the closer to 1 the value is, the better. The remaining indices range between 0 and 1. An excellent model should present high CSI, POD, and HSS values but low FAR, MAE, and RMSE values.

In addition, the baseline method, INCA (Haiden et al., 2011), is compared with CGsNet in forecasting PWGS in CGs. INCA is a nowcasting system developed with complex terrain adaptability at the Austria National Weather Service. In this study, the nowcasts start with a three-dimensional analysis based on a first guess obtained from the output of the numerical weather prediction model (here, the PWAFS model (Li et al., 2016) is used), with observation corrections superimposed. It can provide wind forecasts, for which the update frequency (temporal resolution) is 1 h.

In particular, we concentrate on evaluating ASWS in the range of 8.0-13.9 m/s and PWGS in the range of 10.8-20.8 m/s in CGs events, which has broad value for disaster warning in meteorological operations and aviation applications.

4 Results

4.1 Model performance on ASWS nowcasting

To validate the effectiveness of CGsNet on forecasting ASWS in CGs, the CSI, HSS, POD, FAR, MAE, and RMSE are calculated in Table 2 for the investigated nowcasting lead time. The thresholds at 8.0 m/s, 10.8 m/s and 13.9 m/s of ASWS are evaluated, and the results reveal that CGsNet achieved outstanding performance on these criteria. In detail, for an ASWS threshold of 8.0 m/s, CGsNet has excellent performance with HSS = 0.54, POD = 0.59, MAE = 1.6 m/s, and RMSE = 2.26 m/s. When the threshold is raised to 10.8 m/s, the forecast ability degrades slightly. For strong wind (the threshold is at 13.9

Geoscientific
Model Development
Discussions

m/s), CGsNet still has a certain forecasting ability, with an HSS of 0.20 and a POD of 0.22. This means that the developed CGsNet can retain a decent modeling capability and is useful for ASWS nowcasting in CGs events, especially for strong gusts that are difficult to forecast by traditional methods.

Table 2. Quantitative results of CGsNet on ASWS nowcasting.

ASWS threshold (m/s)	CSI	HSS	POD	FAR	MAE	RMSE
8.0	0.41	0.54	0.59	0.45	1.60	2.26
10.8	0.31	0.42	0.47	0.54	2.19	3.07
13.9	0.15	0.20	0.22	0.61	2.90	4.22

We further investigated the performance of CGsNet by drawing the CSI, HSS, MAE and RMSE curves at all nowcasting
205   lead time stamps. As shown in Figure 4, in the cases with ASWS > 8.0 m/s, the prediction quality gradually decreased as the forecasting time increased. Specifically, the value of CSI/HSS dropped from approximately 0.56/0.70 (lead time at 6 min) to 0.40/0.45 (lead time at 120 min) in the nowcasting results, and the RMSE (MAE) increased from approximately 2.5 (1.7) m/s for the first lead time to 5.1 (3.7) m/s for the last lead time. The case of ASWS > 10.8 m/s (Figure 4b and 4e) is similar to that of ASWS > 8.0 m/s; its prediction quality gradually decreases as the lead time increases, but the performance is degraded
210   compared to that with a threshold of 8.0 m/s.
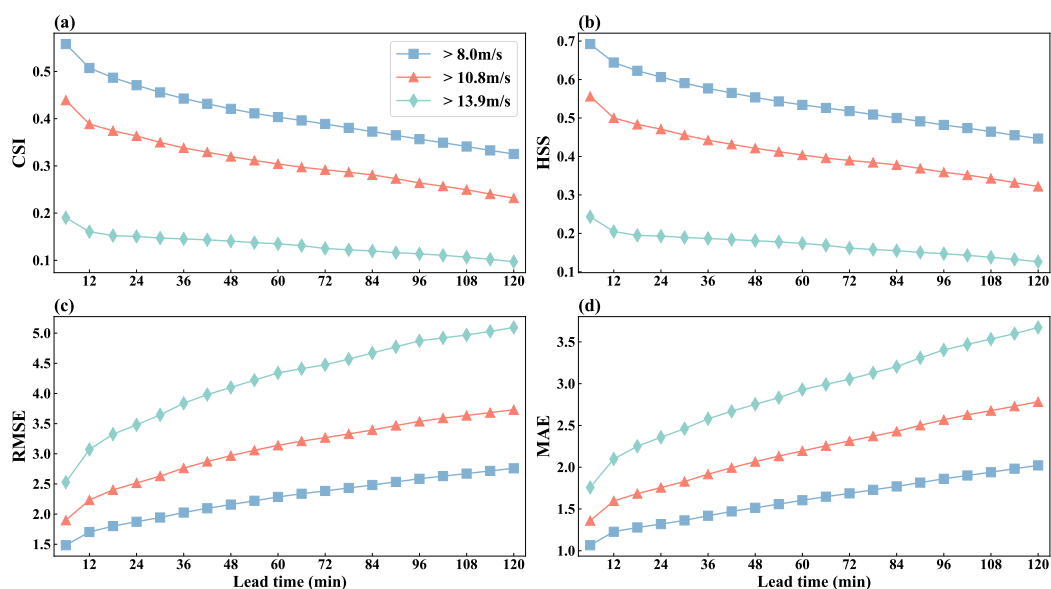
Figure 4. The CGsNet results for different nowcasting lead times of ASWS at thresholds of 8.0 m/s, 10.8 m/s, and 13.9 m/s.

In addition, the evaluation curves are depicted with respect to different nowcasting lead times at the 13.9 m/s threshold. The results are similar to the ASWS at the other two thresholds. In the first 12 minutes, the performance of CGsNet decreased rapidly and then gradually decreased slowly. Although the performance is worse than that with the other two thresholds, CGsNet still exhibits forecasting skill within 2 h. Overall, the above results confirm the effectiveness of the developed CGsNet

215 model, which is skillful for nowcasting ASWS in CGs events.

4.2 Case study of ASWS nowcasting

To further prove the usefulness of CGsNet in detail, we show examples in two meteorologically important weather cases produced by CGsNet. The first case occurred on April 30, 2021, when eastern China was affected by cold air due to the influence of the Northeast Cold Vortex in China. This cold air accompanied by the cold vortex moved eastward and southward,

220 intersecting with some warm and humid air currents in eastern China. Then, the areas along the Yangtze River and north of Jiangsu suffered from SCW, including sudden CGs and hail. Because of the small scale and rapid development of these CGs, numerical models usually cannot forecast this process accurately.

Specifically, hail and large-scale thunderstorms occurred from 18:00 to 22:00 (BJT) in parts of Nantong, Jiangsu, with a maximum wind speed of up to 47.9 m/s in some areas. Figure 5 shows the in situ observations and forecasted ASWS during

225 this period. The CGs developed strongly at 20:12, and the ASWS exceeded 17.2 m/s in some areas. Then, the ASWS gradually decreased after 20:12 for 120 minutes. It is clear that the CGsNet model has good forecasting skill. CGsNet accurately forecasts the position of the CGs and their weakening trend. In particular, the CGsNet model can preserve the strong gust regions (ASWS>10.8 m/s) (Figure 5). The reason for this is that CGsNet employs attention schemes, which better model the short-term and long-term dependency of wind gusts. Additionally, the observed strong gusts continuously moved to the southeast

230 as the lead time continued. CGsNet forecasted this phenomenon precisely, although in the later stage, the locations of the forecasted strong gusts were not exactly the same as in the observations.

The second case is also typical convection weather. It was influenced by the low-level shear lines and strengthened by southwest warm and humid airflow on 15 May 2021. This process occurred in central and eastern Jiangsu, accompanied by heavy precipitation and strong gusts, causing serious economic losses. The observations and forecasts of ASWS for this case

235 are presented in Figure 6.

In the second case, CGs are produced with the development of the squall line in the Jiangsu area. The strong gust position is linearly distributed, moving eastward from western Jiangsu to central Jiangsu between 13:00 and 15:00 (BJT). Figure 6 clearly shows that CGsNet has good forecasting skill for the moving trend due to the improved modeling capability. Additionally, the results demonstrate that CGsNet can accurately forecast the ASWS values in most areas, although the strong gust values are

240 slightly smaller than the observations in some areas. Similar results can also be found in the RMOS forecasts (Figure A1 and A2), which are the other output variables of CGsNet. This further confirms that CGsNet is effective and accurate for ASWS nowcasting. Based on the reliable ASWS forecasts, nowcasting on the PWGS of CGs may be conducted.
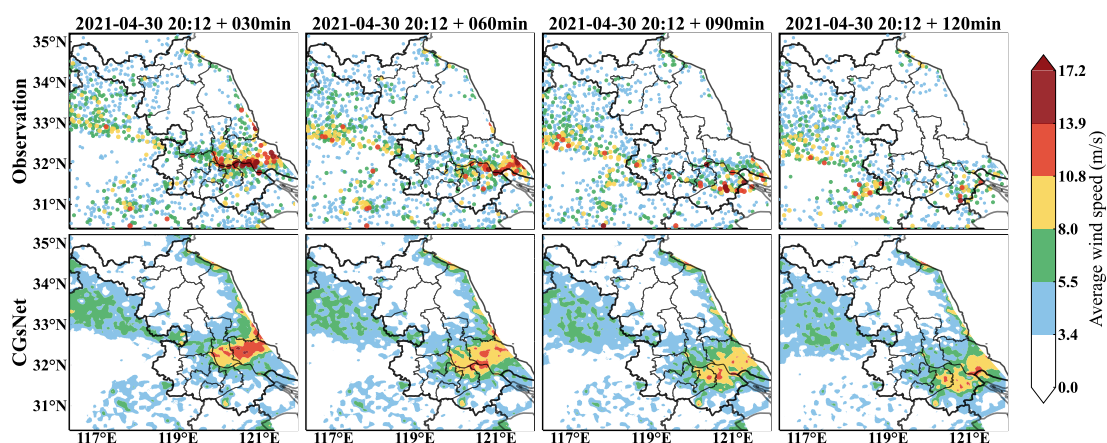
Figure 5. Observations (first row) and forecasts (second row) of ASWS in eastern China, 30 April 2021, 20:12-22:12 BJT. Note that forecasting started at 20:12, and the observations and forecasts are shown at intervals of 30 min.
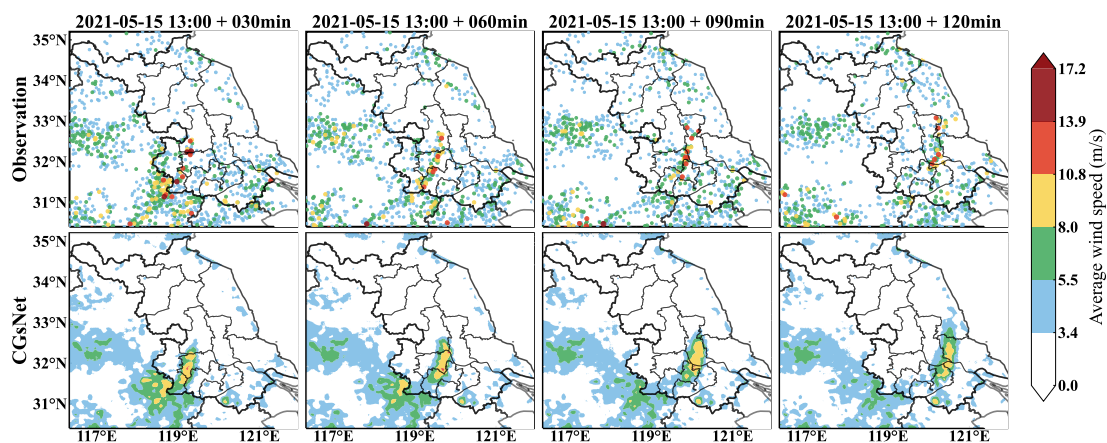
Figure 6. Same as Figure 5, but for 15 May 2021, 13:00-15:00 BJT.

Geoscientific
Model Development
Discussions

EGU

4.3 Peak wind gusts speed nowcasting

ASWS reflects the average speed of CGs, which is not sufficient to determine the actual impact of CGs. The maximum

245 momentary wind speed (e.g., PWGS) can reflect the actual peaks of CGs and is the key factor for the assessment and analysis of weather hazards. Thus, this section focuses on evaluating the reliability and accuracy of CGsNet on nowcasting PWGS.

4.3.1 Gust factor

The gust factor (GF) is the ratio of the wind gust to the wind speed (Harris and Kahl, 2017), and it plays an important role in wind conversion, the practice of converting between average wind speeds over different time periods (Harper et al., 2010).

250 Kahl et al. (2021) showed that gust factors associated with strong winds (>7.65 m/s) were approximately 1.5 in the NW and NNW sectors of Rapid City, South Dakota, and ranged from 1.61 to 2.31 on different directionals at Waukegan. This directional variation in the GF was largely due to the site-specific heterogeneity in surface roughness (Suomi et al., 2013). Harris and Kahl (2017) investigated the GF in Milwaukee, Wisconsin, using Automated Surface Observation System (ASOS) wind measurements from 2007 to 2014 and calculated a mean GF of 1.74. Similarly, we determined the GF using the measured

255 wind data, i.e., ASWS and PWGS observations. Here, we do not consider the direction due to the relatively flat terrain in eastern China; instead, the average GF is explored.

We take the observed maximum ASWS within an hour as the hourly maximum ASWS to match the temporal resolution of the PWGS because the observed PWGS was reported for each hour at all sites in eastern China. Then, the GF is calculated as:

$$GF = \frac{PWGS}{hourly\ maximum\ ASWS} \tag{13}$$

260 According to the above formula, the observed wind data from April to September 2021, including 32015 stations data, were used to calculate the GF. The corresponding scatter plots of the hourly maximum ASWS and PWGS can be found in Figure A3. As a result, we found a GF of 1.77.

4.3.2 Model performance on PWGS nowcasting

Utilizing the calculated GF, we first estimated the 0-2 h PWGS nowcasts by multiplying the GF by the ASWS nowcasts from

265 CGsNet. Then, the PWGS nowcasts were comapared with INCA results to demonstrate the accuracy of CGsNet model and confirm the justifiability of the GF. Note that the results are in one-hour forecasts because the in situ PWGS observations and INCA results are reported for each hour.

The overall evaluation results of CGsNet and INCA on PWGS nowcasting are given in Table 3. The results reveal that CGsNet significantly outperforms INCA on our testing dataset, and it achieved outstanding performance of all criteria. More-

270 over, as the threshold increases, the superiority of CGsNet becomes more and more obviously, e.g, for the PWGS thresholds is 17.2 m/s, CGsNet still keep a decent modeling capability(CSI =0.15, POD=0.25), which is much higher than INCA (CSI =0.03, POD=0.07).

Table 3. Quantitative results of CGsNet and INCA on PWGS nowcasting.

Evaluatation indices	CSI				POD				BIAS				FAR			
PWGS threshold (m/s)	10.8	13.9	17.2	20.8	10.8	13.9	17.2	20.8	10.8	13.9	17.2	20.8	10.8	13.9	17.2	20.8
CGsNet	0.27	0.22	0.15	0.06	0.35	0.31	0.25	0.12	0.63	0.73	0.94	1.21	0.45	0.57	0.73	0.90
INCA	0.11	0.06	0.03	0.02	0.30	0.13	0.07	0.04	2.07	1.51	1.27	1.14	0.85	0.91	0.94	0.96

For a more detailed comparison, the the PWGS results from CGsNet and INCA for 0-2 h nowcasting lead times at different thresholds are showed in Table 4. At the lead time of 0-1 h, the CSI and POD of CGsNet always keep top positions at different thresholds. Meanwhile, the BIAS and FAR of CGsNet are also lower than those of INCA. Besides, the quality of CGsNet and INCA both degraded with the forecasting time increasing. Specifically, the performance of CGsNet still keep a forecasting skill at the lead time of 1-2 h, while INCA is similar to the first hour, it is lack of skill, the CSI at all thresholds are lower than 0.1. It's worth noting that the POD of INCA at the threshold of 10.8 m/s is a little larger than the CGsNet (0.29 vs. 0.28) at the lead time of 1-2 h.This is due to the high false alarm ratio of INCA, thus, it has the high FAR and BIAS. Overall, the results indicate that the developed CGsNet is helpful to improve the accuracy of CGs nowcasting and more skillful than INCA.

Table 4. The PWGS evaluation results from CGsNet and INCA for different nowcasting lead times at thresholds of 10.8 m/s, 13.9 m/s, 17.2 m/s and 20.8 m/s.

| Lead time of 0-1 h																
Evaluatation indices	CSI				POD				BIAS				FAR			
PWGS threshold (m/s)	10.8	13.9	17.2	20.8	10.8	13.9	17.2	20.8	10.8	13.9	17.2	20.8	10.8	13.9	17.2	20.8
CGsNet	0.31	0.26	0.17	0.06	0.40	0.37	0.28	0.14	0.69	0.79	0.99	1.43	0.42	0.53	0.71	0.90
INCA	0.13	0.06	0.04	0.02	0.31	0.13	0.07	0.03	1.74	1.30	1.10	1.00	0.82	0.90	0.93	0.97
Lead time of 1-2 h																
Evaluatation indices	CSI				POD				BIAS				FAR			
PWGS threshold (m/s)	10.8	13.9	17.2	20.8	10.8	13.9	17.2	20.8	10.8	13.9	17.2	20.8	10.8	13.9	17.2	20.8
CGsNet	0.22	0.18	0.13	0.05	0.28	0.26	0.21	0.09	0.56	0.66	0.88	0.98	0.49	0.61	0.76	0.91
INCA	0.09	0.05	0.03	0.02	0.29	0.14	0.07	0.05	2.43	1.73	1.45	1.29	0.88	0.92	0.95	0.96

4.3.3 Case study of PWGS nowcasting

To illustrate the perfromance of CGsNet more intuitively, the INCA forecasts in two instances are presented for comparison. The first case is on June 23, 2022, short-term heavy precipitation and CGs occurred over a large area in Jiangsu Province because of the influence of the Northeast Cold Vortex in China. As shown in Figure 7, for the first nowcasting hour (19:00 BJT), the CGs were mainly located in central Jiangsu, and the PWGS at some sites exceeded 20.8 m/s. Then, the CGs moved

to the southeast of Jiangsu from 19:00 to 20:00 (BJT), occurring in Nantong and surrounding areas, and the PWGS gradually decreased. During this process, it is clear that CGsNet can effectively forecast the location of the CGs, especially for the first hour of nowcasting (19:00 BJT). However, CGsNet underestimates the PWGS at some sites. INCA does not accurately forecast the occurrence of CGs at 19:00 (BJT); the area in which PWGS > 17.2 m/s is too small, and the PWGS is also significantly

290　underestimated. Besides, INCA failed to forecast the occurrence of CGs at 20:00 (BJT), and the forecasted PWGS values were all below 17.2 m/s.
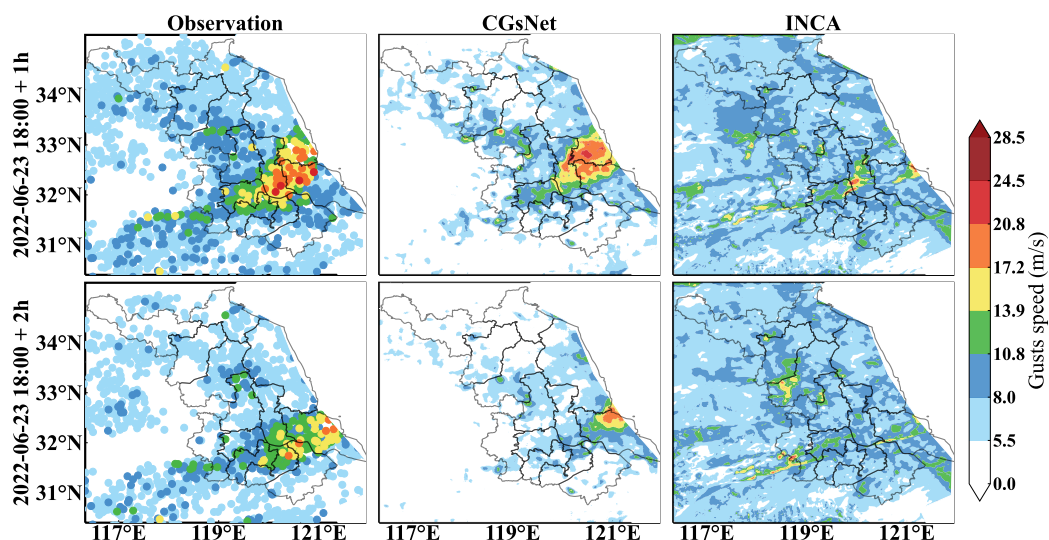

Figure 7. Observations and forecasts of PWGS in eastern China on June 23, 2022, 18:00-20:00 BJT. Note that the forecasting started at 18:00. The first column shows the observations at 19:00 BJT and 20:00 BJT. The last two columns show the PWGS forecasts obtained by CGsNet and INCA.

The performance of CGsNet and INCA at different PWGS thresholds for the case on on June 23, 2022 are shown in Figure 8. In particular, the PWGS at thresholds of 10.8 m/s, 13.9 m/s and 17.2 m/s is compared because the PWGS is below 20.8 m/s over most of the study area at 20:00 (BJT). The performance of CGsNet and INCA both decrease as the threshold of PWGS

295　increases, but CGsNet significantly outperforms INCA. For example, in the cases of PWGS > 10.8 m/s, CGsNet achieved outstanding performance on the criteria, with a CSI of 0.34, a POD of 0.43, and a FAR of 0.38, which are higher than the corresponding INCA values (CSI=0.15, POD=0.26, and FAR=0.73). It is worth noting that the BIAS of CGsNet (0.70) is worse than that of INCA (0.97) at a threshold of 10.8 m/s, which may be because some areas with PWGS < 10.8 m/s are mispredicted by INCA as PWGS > 10.8 m/s. In this condition, the BIAS of INCA is small, but the performance on FAR and

300　POD is poor. Again, the advantages of CGsNet become increasingly obvious with increasing PWGS threshold (13.9 m/s and

17.2 m/s); in particular, for PWGS > 17.2 m/s, INCA is nearly unable to perform CGs nowcasting, while CGsNet still shows nowcasting skill.
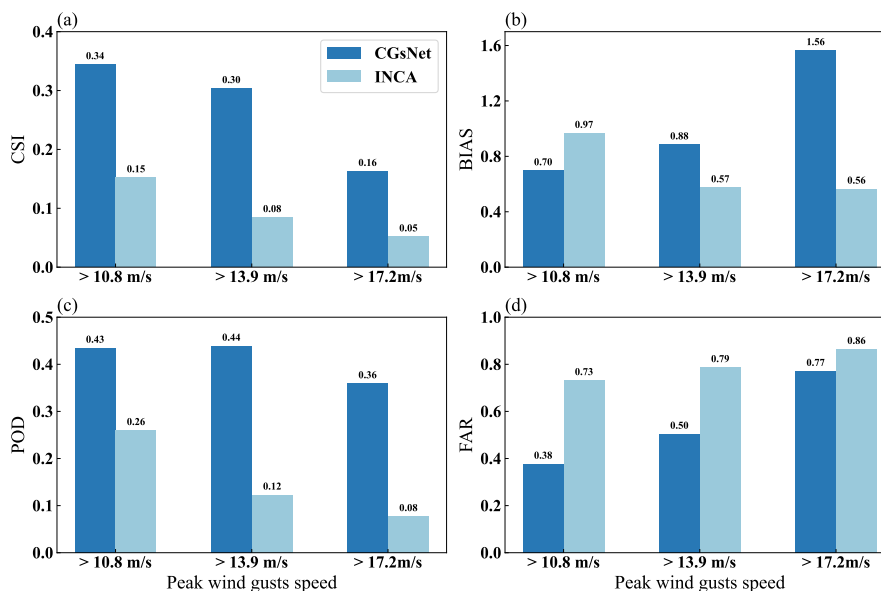

Figure 8. Comparison results of CGsNet and INCA on PWGS at thresholds of 10.8 m/s, 13.9 m/s, and 17.2 m/s on June 23, 2022, 18:00-20:00 BJT.

The other CGs case on 26 July 2022 was also selected to further verify the nowcasting ability of the CGsNet model. For this case, with the movement and development derecho in eastern China, Jiangsu and northern Zhejiang were hit by SCW (i.e.,
305 CGs, short-term heavy precipitation and tornadoes). Figure 9 shows the observed and forecasted PWGS. Specifically, central and southern Jiangsu suffered from CGs during 14:00-16:00 (BJT), and there was PWGS > 28.5 m/s in some areas. From 15:00 to 16:00 (BJT), the CGs gradually moved eastward with slight weakening. Compared with the observations, CGsNet was shown to be accurate in capturing the location of the CGs, despite underestimating the PWGS, which was greater than 20.8 m/s. INCA did not accurately forecast the area where the CGs would occur and underestimated the PWGS. In addition,
310 neither CGsNet nor INCA accurately forecasted the CGs that occurred in northern Zhejiang at 15:00 and 16:00 (BJT); the CGsNet forecasts were weaker than the observations, while the INCA forecasts were in the wrong area. Overall, the results demonstrate that CGsNet is better than INCA and shows excellent performance in CGs nowcasting.

In addition, Figure 10 shows the performance of CGsNet and INCA at different PWGS thresholds. Unlike the first case, we evaluate the PWGS at a threshold of 20.8 m/s, since many sites have PWGS > 20.8 m/s in this case. The results indicate that
315 the CSI and POD of both methods show a general decrease with increasing thresholds, and the BIAS and FAR increase. The CGsNet forecasts achieve better performance than those of INCA at all thresholds; e.g., the evaluated POD reaches 0.51 when the threshold is 17.2 m/s, which is 147.62% higher than that of INCA. Additionally, INCA has a poor performance on CSI and FAR at each PWGS threshold, which is due to the large location deviation of the INCA forecasts with respect to where
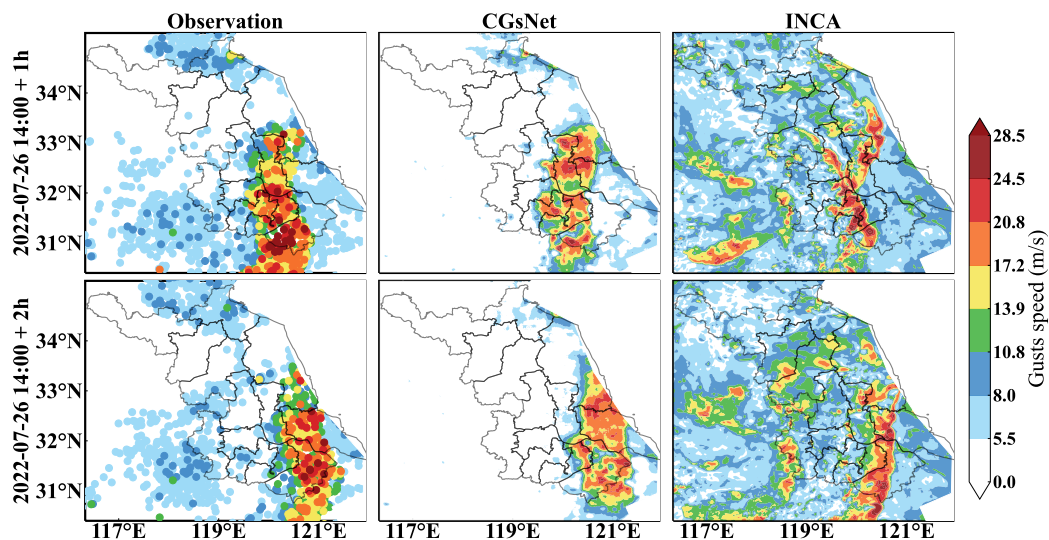
Figure 9. Same as Fig. 7, but for July 26, 2022, 14:00-16:00 BJT.

CGs occurred. Again, the result illustrates the usefulness of the proposed CGsNet in CGs nowcasting. It also demonstrates the
320 effectiveness of the GF.
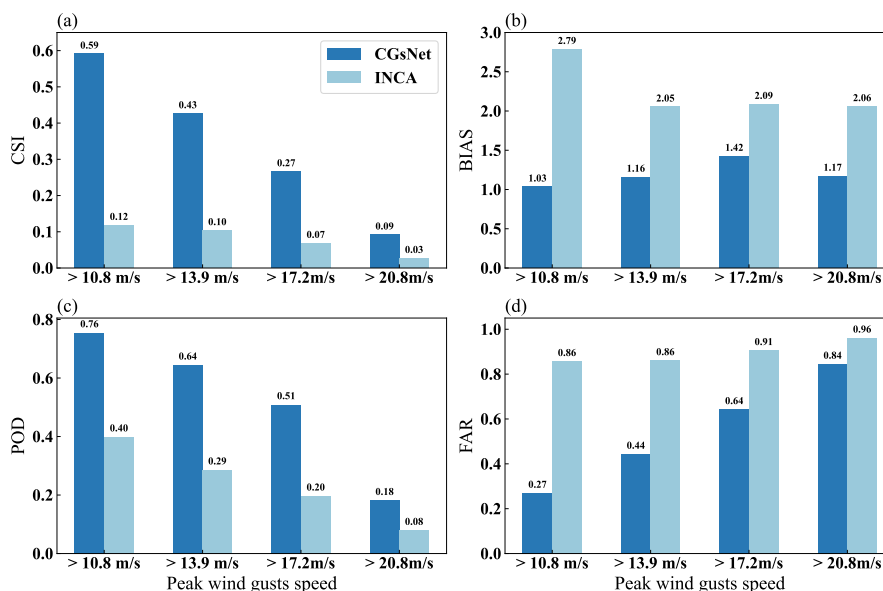
Figure 10. Same as Fig. 8, but for July 26, 2022, 14:00-16:00 BJT.

5 Discussion and conclusions

In this study, a physics-constrained deep learning model was proposed for CGs nowcasting. This model was established based on the extended PhyDNet and is called CGsNet. Then, by using observed ASWS and RMOS datasets, CGsNet was trained for CGs nowcasting in eastern China. CGsNet can produce ASWS nowcasts of 6-120 min with a temporal resolution of 6 min
325 and a spatial resolution of 1 km. To estimate the PWGS forecasts, we multiplied the forecasted ASWS by the GF, which was determined from the ratio of the historical observed ASWS to the PWGS. The PWGS forecasts had the same spatiotemporal resolution as the ASWS forecasts. This is the first time that minute-level CGs nowcasting has been achieved for eastern China.

Several metrics for evaluating the performance of CGsNet were analyzed, confirming the effectiveness of the CGsNet model for ASWS and PWGS nowcasting. The PWGS forecasts were also compared with the INCA results, and the results demon-
330 strated that the performance of CGsNet is better than that of INCA. CGsNet can effectively forecast the location and evolution of CGs, and the PWGS forecasts are a good match with the observations. In contrast, INCA does not accurately determine the locations and strengths of CGs, with low POD and CSI and high BIAS and FAR. The superiority of the PWGS results also proves that the calculated GF is reliable.

In addition to these achievements, there are some points requiring further discussion and investigation. For example, CGsNet
335 sometimes underestimates the intensity of ASWS and PWGS, which may be caused by several different factors. For ASWS forecasts, this may be due to the limited modeling ability of CGsNet; that is, the model has not fully learned the nonlinear variation characteristics of CGs. In addition, the input variables may be insufficient, and it is difficult to accurately forecast small-scale and nonstationary CGs with only radar data and observed wind data. For PWGS forecasts, the error from ASWS and GF, and thus their combination, leads to the deviation of the predicted PWGS.

340 Therefore, in future work, more meteorological factors related to CGs, such as the three-hour pressure change and relative humidity, should be considered in CGs nowcasting. The predictive ability of the model can then be improved to some extent by reforming the training dataset. In addition, a more accurate GF should be calculated by using years of wind observations. Although our experiments were performed in eastern China, the proposed CGs nowcasting technology can be generalized to a wide range of areas. Besides, CGs nowcasting technology could also be applied to forecast other phenomena, such as
345 convection or hail, for which real-time-response models are crucially needed.

Code availability. The source code and the used data are available at this repository https://doi.org/10.7910/DVN/PIZU7V.
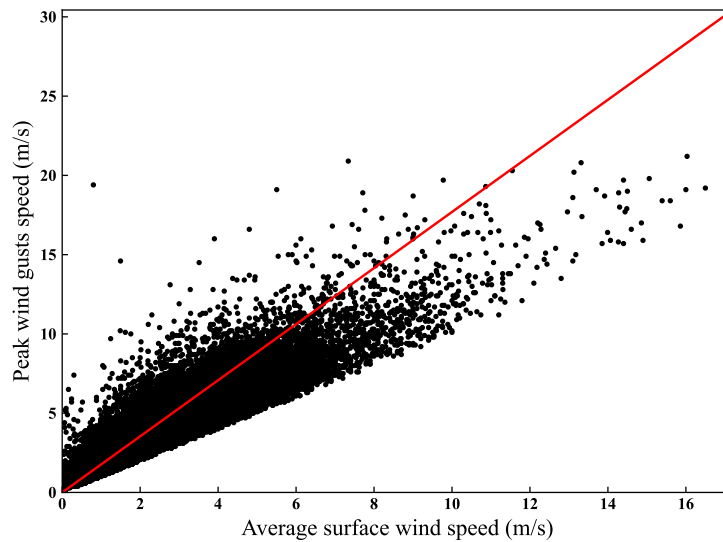
Appendix A: appendix figures
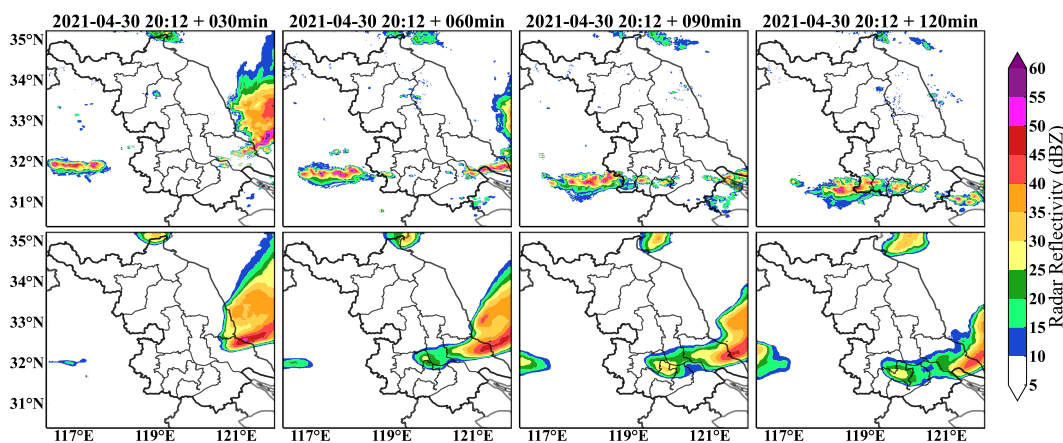
Figure A1. Observations (first row) and forecasts (second row) of ROMS in eastern China, 30 April 2021, 20:12-22:12 BJT. Note that forecasting started at 20:12, and the observations and forecasts are shown for every 30 min.
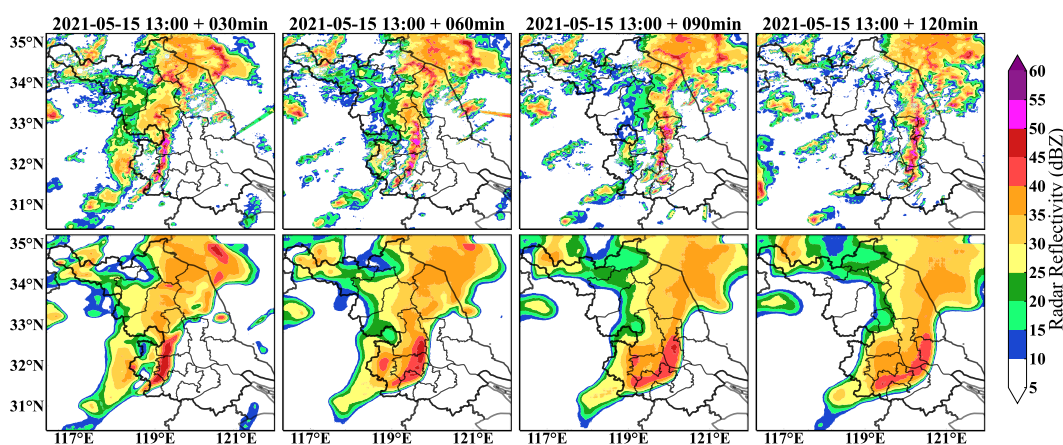
Figure A2. Same as Figure A1, but for 15 May 2021, 13:00-15:00 BJT.

Figure A3. Scatter plot of the hourly maximum ASWS and PWGS. The red line represents the linear regression line for the GF.

Author contributions. Haixia Xiao was responsible for writing the original draft and completing the result analysis. Yaqiang Wang directed the study and wrote and reviewed the paper. Yu Zheng was responsible for developing the CGsNet model and visualizing the results. Yuanyuan Zheng provided useful comments on this study. The INCA and AWS datasets were processed by Xiaoran Zhuang. The RMOS data were acquired and processed by Hongyan Wang and Mei Gao.

350

Competing interests. The authors declare that they have no conflicts of interest.

355

Geoscientific
Model Development
Discussions

References

Chaudhuri, S. and Middey, A.: Adaptive neuro-fuzzy inference system to forecast peak gust speed during thunderstorms, Meteorology and Atmospheric Physics, 114, 139–149, https://doi.org/10.1007/s00703-011-0158-4, 2011.

Danandeh Mehr, A., Rikhtehgar Ghiasi, A., Yaseen, Z. M., Sorman, A. U., and Abualigah, L.: A novel intelligent deep learning predictive model for meteorological drought forecasting, Journal of Ambient Intelligence and Humanized Computing, pp. 1–15, https://doi.org/s12652-022-03701-7, 2022.

Doswell, C. A.: Severe convective storms—An overview, Severe convective storms, pp. 1–26, https://doi.org/10.1007/978-1-935704-06-5_1, 2001.

Doswell, C. A., Brooks, H. E., and Maddox, R. A.: Flash Flood Forecasting: An Ingredients-Based Methodology, Weather and Forecasting, 11, 560–581, https://doi.org/10.1175/1520-0434(1996)01160;0560:fffaib62;2.0.co;2, 1996.

Duan, M., Xia, J., Yan, Z., Han, L., Zhang, L., Xia, H., and Yu, S.: Reconstruction of the Radar Reflectivity of Convective Storms Based on Deep Learning and Himawari-8 Observations, Remote Sensing, 13, 3330, https://doi.org/10.3390/rs13163330, 2021.

Franch, G., Nerini, D., Pendesini, M., Coviello, L., Jurman, G., and Furlanello, C.: Precipitation Nowcasting with Orographic Enhanced Stacked Generalization: Improving Deep Learning Predictions on Extreme Events, Atmosphere, 11, https://doi.org/10.3390/atmos11030267, 2020.

Fujita, T. T.: Downbursts: meteorological features and wind field characteristics, Journal of wind engineering and industrial aerodynamics, 36, 75–86, https://doi.org/10.1016/0167-6105(90)90294-M, 1990.

Guen, V. L. and Thome, N.: A deep physical model for solar irradiance forecasting with fisheye images, in: Proceedings of the IEEE/CVF Conference on Computer Vision and Pattern Recognition Workshops, pp. 630–631, https://doi.org/10.1016/0167-6105(90)90294-M, 2020a.

Guen, V. L. and Thome, N.: Disentangling physical dynamics from unknown factors for unsupervised video prediction, in: Proceedings of the IEEE/CVF Conference on Computer Vision and Pattern Recognition, pp. 11 474–11 484, https://doi.org/10.1109/CVPR42600.2020.01149, 2020b.

Haiden, T., Kann, A., Wittmann, C., Pistotnik, G., Bica, B., and Gruber, C.: The Integrated Nowcasting through Comprehensive Analysis (INCA) system and its validation over the Eastern Alpine region, Weather and Forecasting, 26, 166–183, https://doi.org/10.1175/2010WAF2222451.1, 2011.

Harper, B., Kepert, J., and Ginger, J.: Guidelines for converting between various wind averaging periods in tropical cyclone conditions, Geneva, Switzerland: WMO, 2010.

Harris, A. R. and Kahl, J. D.: Gust factors: Meteorologically stratified climatology, data artifacts, and utility in forecasting peak gusts, Journal of Applied Meteorology and Climatology, 56, 3151–3166, https://doi.org/10.1175/JAMC-D-17-0133.1, 2017.

Holleman, I.: Estimation of the maximum velocity of convective wind gusts, Internal KNMI report, 2001.

Jahanbakht, M., Xiang, W., Robson, B., and Azghadi, M. R.: Nitrogen prediction in the Great Barrier Reef using finite element analysis with deep neural networks, Environmental Modelling & Software, 150, 105 311, https://doi.org/10.1016/j.envsoft.2022.105311, 2022.

Kahl, J. D.: Forecasting peak wind gusts using meteorologically stratified gust factors and MOS guidance, Weather and Forecasting, 35, 1129–1143, https://doi.org/10.1175/WAF-D-20-0045.1, 2020.

Kahl, J. D., Selbig, B. R., and Harris, A. R.: Meteorologically Stratified Gust Factors for Forecasting Peak Wind Gusts across the United States, Bulletin of the American Meteorological Society, 102, E1665–E1671, https://doi.org/10.1175/BAMS-D-21-0013.1, 2021.

Kingma, D. P. and Ba, J.: Adam: A method for stochastic optimization, arXiv preprint arXiv:1412.6980, https://doi.org/10.48550/arXiv.1412.6980, 2014.

395 Knupp, K. R.: Downdrafts within high plains cumulonimbi. Part I: General kinematic structure, Journal of Atmospheric Sciences, 44, 987–1008, https://doi.org/10.1175/1520-0469(1987)0442.0.CO;2, 1987.

Kolendowicz, L., Taszarek, M., and Czernecki, B.: Convective and non-convective wind gusts in Poland, 2001-2015, Meteorology Hydrology and Water Management. Research and Operational Applications, 4, 15–21, https://doi.org/10.26491/mhwm/63636, 2016.

Lagerquist, R., McGovern, A., and Smith, T.: Machine learning for real-time prediction of damaging straight-line convective wind, Weather
400 and Forecasting, 32, 2175–2193, https://doi.org/10.1175/WAF-D-17-0038.1, 2017.

Lei, M., Shiyan, L., Chuanwen, J., Hongling, L., and Yan, Z.: A review on the forecasting of wind speed and generated power, Renewable and sustainable energy reviews, 13, 915–920, https://doi.org/10.1016/j.rser.2008.02.002, 2009.

Li, X., Zeng, M., Wang, Y., Wang, W., Wu, H., and Mei, H.: Evaluation of two momentum control variable schemes and their impact on the variational assimilation of radarwind data: Case study of a squall line, Advances in Atmospheric Sciences, 33, 1143–1157,
405 https://doi.org/10.1007/s00376-016-5255-3, 2016.

McNulty, R. P.: Severe and convective weather: A central region forecasting challenge, Weather and Forecasting, 10, 187–202, https://doi.org/10.1175/1520-0434(1995)010<0187:sacwac>2.0.co;2, 1995.

Mohr, S., Kunz, M., Richter, A., and Ruck, B.: Statistical characteristics of convective wind gusts in Germany, Natural Hazards and Earth System Sciences, 17, 957–969, https://doi.org/10.5194/nhess-17-957-2017, 2017.

410 Nerini, D., Buzzi, M., and Trefalt, S.: Nowcasting of North Foehn wind gusts in Switzerland using AdaBoosting, in: World Weather Open Science Conference, 2014.

Niu, Z., Zhong, G., and Yu, H.: A review on the attention mechanism of deep learning, Neurocomputing, 452, 48–62, https://doi.org/10.1016/j.neucom.2021.03.091, 2021.

Ray, P.: Mesoscale meteorology and forecasting, Springer, 2015.

415 Sadeghi, M., Nguyen, P., Hsu, K., and Sorooshian, S.: Improving near real-time precipitation estimation using a U-Net convolutional neural network and geographical information, Environmental Modelling & Software, 134, 104 856, https://doi.org/10.1016/j.envsoft.2020.104856, 2020.

Sheng, C., Gao, S., and Xue, M.: Short-range prediction of a heavy precipitation event by assimilating Chinese CINRAD-SA radar reflectivity data using complex cloud analysis, Meteorology and Atmospheric Physics, 94, 167–183, https://doi.org/10.1007/s00703-005-0177-0,
420 2006.

Sheridan, P.: Current gust forecasting techniques, developments and challenges, Advances in Science and Research, 15, 159–172, https://doi.org/10.5194/asr-15-159-2018, 2018.

Shi, X., Chen, Z., Wang, H., Yeung, D.-Y., Wong, W.-K., and Woo, W.-c.: Convolutional LSTM network: A machine learning approach for precipitation nowcasting, Advances in neural information processing systems, 28, https://doi.org/10.1007/978-3-319-21233-3_6, 2015.

425 Shi, X., Gao, Z., Lausen, L., Wang, H., Yeung, D.-Y., Wong, W.-k., and Woo, W.-c.: Deep learning for precipitation nowcasting: A benchmark and a new model, Advances in neural information processing systems, 30, https://doi.org/10.48550/arXiv.1706.03458, 2017.

Stensrud, D. J., Xue, M., Wicker, L. J., Kelleher, K. E., Foster, M. P., Schaefer, J. T., Schneider, R. S., Benjamin, S. G., Weygandt, S. S., Ferree, J. T., et al.: Convective-scale warn-on-forecast system: A vision for 2020, Bulletin of the American Meteorological Society, 90, 1487–1500, https://doi.org/10.1175/2009BAMS2795.1, 2009.

430   Suomi, I., Vihma, T., Gryning, S.-E., and Fortelius, C.: Wind-gust parametrizations at heights relevant for wind energy: A study based on mast observations, Quarterly Journal of the Royal Meteorological Society, 139, 1298–1310, https://doi.org/10.1002/qj.2039, 2013.

Tran, Q.-K. and Song, S.-k.: Computer vision in precipitation nowcasting: Applying image quality assessment metrics for training deep neural networks, Atmosphere, 10, 244, https://doi.org/10.3390/atmos10050244, 2019.

Veillette, M., Samsi, S., and Mattioli, C.: Sevir: A storm event imagery dataset for deep learning applications in radar and satellite meteorol-

435   ogy, Advances in Neural Information Processing Systems, 33, 22 009–22 019, 2020.

Wakimoto, R. M.: Convectively driven high wind events, in: Severe convective storms, pp. 255–298, Springer, https://doi.org/10.1007/978-1-935704-06-5_7, 2001.

Wang, F., Yu, X., Pei, Y., Yang, X., Meng, K., and He, L.: Radar echo characteristics of thunderstorm gales and forecast key points in Hebei Province, Journal of Applied Meteorological Science, 27, 342–351, 2016.

440   Wang, H., Zhang, Y.-M., Mao, J.-X., and Wan, H.-P.: A probabilistic approach for short-term prediction of wind gust speed using ensemble learning, Journal of Wind Engineering and Industrial Aerodynamics, 202, 104 198, https://doi.org/10.1016/j.jweia.2020.104198, 2020.

WMO: Measurements of surface wind, Guide to meteorological instruments and methods of observation, WMO-No.8, World Meteorological Organization, Genewa, 2010.

Yang, X., Sun, J., and Zheng, Y.: A 5-yr climatology of severe convective wind events over China, Weather and Forecasting, 32, 1289–1299,

445   https://doi.org/10.1175/WAF-D-16-0101.1, 2017.

Yu, X. and Zheng, Y.: Advances in severe convection research and operation in China, Journal of Meteorological Research, 34, 189–217, https://doi.org/10.1007/s13351-020-9875-2, 2020.

Yuan, Y., Wang, P., Wang, D., and Jia, H.: An algorithm for automated identification of gust fronts from Doppler radar data, Journal of Meteorological Research, 32, 444–455, https://doi.org/10.1007/s13351-018-7089-7, 2018.

450   Zhou, K., Zheng, Y., Li, B., Dong, W., and Zhang, X.: Forecasting different types of convective weather: A deep learning approach, Journal of Meteorological Research, 33, 797–809, https://doi.org/10.1007/s13351-019-8162-6, 2019.